Faculty of Science

MIGRATION OF FLUID DURING DEFORMATION OF MOLTEN DEUTRATED ICE USING 3D IMAGE ANALYSIS

Uzochukwu Damian Akwuba

Degree of Master of Science (120 credits)
with a major in Earth Sciences
45 hec

Department of Earth Sciences
University of Gothenburg
2021 B1150

UNIVERSITY OF GOTHENBURG

UNIVERSITY OF GOTHENBURG
Department of Earth Sciences
Geovetarcentrum/Earth Science Centre

MIGRATION OF FLUID DURING DEFORMATION OF MOLTEN DEUTRATED ICE USING 3D IMAGE ANALYSIS

Uzochukwu Damian Akwuba

ISSN 1400-3821

B1150
Master of Science (120 credits) thesis
Göteborg 2021

Mailing address
Geovetarcentrum
S 405 30 Göteborg

Address
Geovetarcentrum
Guldhedsgatan 5A

Telephone
031-786 19 56

Geovetarcentrum
Göteborg University
S-405 30 Göteborg
SWEDEN

ABSTRACT

The behaviour of infiltrating and intergranular fluid in an ice body is essential in understanding the deflection of the glacier body. The movement of the fluid during deformation is most naturally controlled by compressive stress and temperature gradient which is important in understanding the behaviour of the glacier body. 3D direct imaging technique was used to observe and analyse 3 samples of deutrated ice. This was done to obtain statistical and morphological topology of the samples. From analysis of the samples, heterogeneous fluid flow was observed from the image rendering of the deformed sample and the style of fluid flow depended on the dominant mechanism of hydrostatic pressure and fluid reaction that drive permeability. Based on the observation from this method, the distribution of the fluid pathways is influenced by changes in stress and strain localization.

Ice: *Deformation*, *Tomography*, *Fluid Migration*, *Fractures*

ACKNOWLEDGEMENTS

The grant from Adlerbertska schloraship is greatly appreciated for making my Master's programme a success. Big thanks to my supervisor Mark Peternell for his support and guidance throughout the period of this thesis. I also want to appreciate Dr, Frider Enzmann and Carina Liebl for their support during my stay in Germany. Special thanks to Anthony Okorie for his support especially during my writing process.

CONTENTS

LIST OF FIGURES

LIST OF TABLES

1 BACKGROUND

1.1 Introduction

Melt water close to the base of the Greenland ice body migrate upwards during deformation and cause a refreezing of the ice body. This refrozen section of the ice body which is about 1.1k in Greenland causes a deflection in the stratigraphy of the ice sheet(Bell et al., 2014). The basal units along the ice sheet margin and within the interior are found to contain refrozen melt water, but the feature and pathway of migration is not fully understood(Bell et al., 2014). Temperature difference between the cooled phase interface and the superheated melt feed was thought to be the driving force for the migration of fluid during hot deformation of material (Henning & Ulrich, 1997; Pfann, 1955). As a result of diffusion of the excited crystals across the solid phase. Further studies by Kingery and Goodnow, 1963 suggested that brine diffusion though occurring in nature but is less significant than bulk drainage through interconnected channels. Recent studies on the deformation of continental crust suggest that melting begins at the grain boundary where reactant minerals touch each other (Mehnert et al., 1973; Sawyer, 2001).

The grain boundaries of polycrystalline ice contains water molecules which are more densely packed than within the ice crystals (Faria et al., 2014b). The grain boundaries get more connected during grain boundary migration. Normal grain boundary migration has been identified as the main way of deformation in the basal unit of the ice sheet(Wilson et al., 2015; Wilson et al., 2014) leaving behind pores which are greater 50um(Azuma et al., 2012; Weikusat et al., 2009). The motion of grain boundaries in firn and bubbly ice is strongly affected by a number of influences like stored strain energy, bubbles and a non-steady-state configuration of the grain boundary network. The pinning of of the grain boundary during migration by bubble and other impurities is another influence on the grain boundary migration. During deformation heat is usually generated by geothermal heat at the base of the ice and this causes melt in the ice. Nye, 1989 experimental research proved that water is found at the three grain intersections and connect to four grain intersection which invariably aid in the permeability of ice by creating capillary channels along the three grain boundary. Because melting starts at the grain boundary, the temperature at which melting occurs usually

depend on the stress applied, the interfacial free energies, the salt content of the liquid phases and the nature of the defect(Lliboutry, 1971; Sawyer, 2001).

Ice is considered a rock and a mineral because of its crystalline nature. Which is basic reasons why we perform experiments using ice and extrapolating it to rheological behaviour of ice in polar ice sheet (Middleton et al., 2017) and comparing it with mechanical behaviour of rocks close to their melting temperature (Faria et al., 2014b). Although Ice is not as ubiquitous as quartz nor as precious as diamond but is highly regarded for its economic and environmental importance (Faria et al., 2010). Sea ice and glacier ice are the most common kinds of ice on earth. Sea ice occupy vast area of the ocean surface especially in the polar region while glacier ice occupy vast surface areas on land especially during winter period and more permanently in high altitude areas and polar regions of the earth . The formation processes for both can be different. Sea ice forms from the solidification of liquid water at freezing temperature over the sea, while glacier ice forms from the sintering and densification of snow on land through various thermodynamic processes. It takes hundreds to thousands of years for snow to transform from snow to firn before becoming bubble free glacier ice (Schulson & Duval, 2009; Staroszczyk et al., 2019). The ice cover in these area determine to a great extent the amount of solar energy absorbed by the Earth, as well as the heat and water transfer in the atmosphere. It is also excellent analogy to the study of the deformation processes that happens in the Earth's interior (Faria et al., 2014a; Wilson et al., 2014). The rheological behaviour and deformation mechanisms of this form of ice has not yet been fully understood, so when considering these processes that occur in these environment, rheological properties are determined in controlled laboratory experiments and then extrapolated to conditions found in nature using flow laws(Glen, 1955; Middleton et al., 2017). The correct intepretation of the microstructure and crystallographic preferred orientation(CPO) of crystals during deformation is critical in understanding the bulk rheology of glacier ice (Piazolo et al., 2013; Wilson et al., 2014). Interestingly, this rheological properties that occur in these environment can be determined in laboratory controlled environment and extrapolated to conditions found in nature. Study of creep in ice is a good insight on hot deformation within the earth crust and it is beneficial because it is accessible and has has low melting temperature and can easily be managed in the lab(Faria et al., 2014b).

In this study, the distribution of Pores in a 3D tomography image of D_2O ice and the segemented redristributed melt water after partial deformation at $+2^0C$ is analyzed. D_2O ice is used as a replacement for H_2O in experiments carried out in neutron beam lines where replacement of H_2O by D_2O is necessary to avoid incoherent scattering of diffracted beam. These in-situ studies have allowed the evolution of textures during

deformation to be observed and grain scale changes linked to the dominant deformation mechanism to be identified (Wilson et al., 2015; Wilson et al., 2014). In this report, the result from neutron tomography imaging done in Australia is analyzed to observe the deformation processes of ice when stress is applied and temperature is increased. The purpose of the project is aimed at studying the pathway for the migration of fluid by analyzing the microstructure of deformed and underformed sample. The method allows us to follow the fluid and its propagation both on surface and in the volume allowing us to identify the relations between deformation microstructure and the propagation of fluid in the in-situ deformation experiment done on a mixture of heavy water D_2O and normal water H_2O using neutron tomography. Analyzing the movement of reactant fluid through the whole mixture using this as analogy to the movement of melt through rock in nature. For the purpose of writing, 'Fluid and Melt' will be used interchangeable for ease of communication.

1.2 Properties of Ice

This section deals on the fundamental physical properties of ice with emphasis on its mechanical properties. It is a brief description of the microstructure of Ice concentrating on the most important properties of individual ice crystals.

Ice is water in a solid state and can exist both in a crystalline and amorphous form. On planet earth, the crystalline form of ice exist in different form also 1h and 1c. The amorphous form of ice can be found in the extra- terrestrial planet like the satellite of Jupiter Europa and in the coldest part of our atmosphere and can also be produced in the laboratory (Bartels-Rausch et al., 2012).

Figure 1.1 illustrate the different crystalline form of ice based on researches and it follows based from the phase diagram that the highest possible pressure to which the ice is subjected on earth are those occurring at the bottom of Antarctica at a depth of about 4800m and pressure of about 45GPa. Therefore it goes to say that the highest possible pressure for for ice to form on planet Earth is ice 1 (Staroszczyk et al., 2019). Depending on the orientation of the oxygen atom in the ice, it can exist in two forms, hexagonal ice(1h) and cubic ice (1c). Hexagonal ice is formed when liquid water is cooled down to 0^0C at earth's normal atmospheric pressure while the cubic ice is a rare form in which the oxygen atoms are arranged in a diamond structure . It can be made in a laboratory at temperature between -143^0C and -53^0C(Schulson & Duval, 2009; Staroszczyk et al., 2019). Like the amorphous ice, some traces of ice 1c can be present in the upper layers of the Earth's atmosphere(Bartels-Rausch et al., 2012). As the whole work will be centered on laboratory prepared ice, which is made by reducing

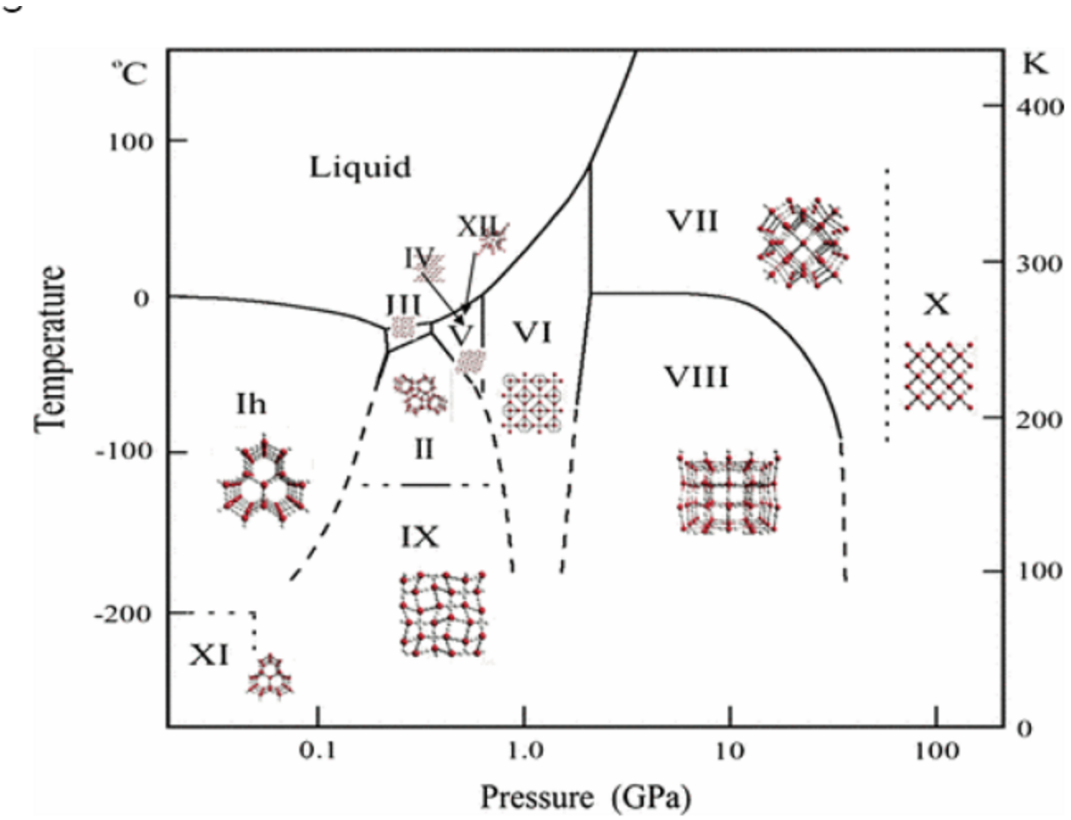

Figure 1.1: Illustrating the different forms of water adopted from (Bartels-Rausch et al., 2012) From the phase diagram the only form of ice existing on Earth is ice 1 while the others can be produced in the laboratory or observed on the surface of extra terrestrial bodies

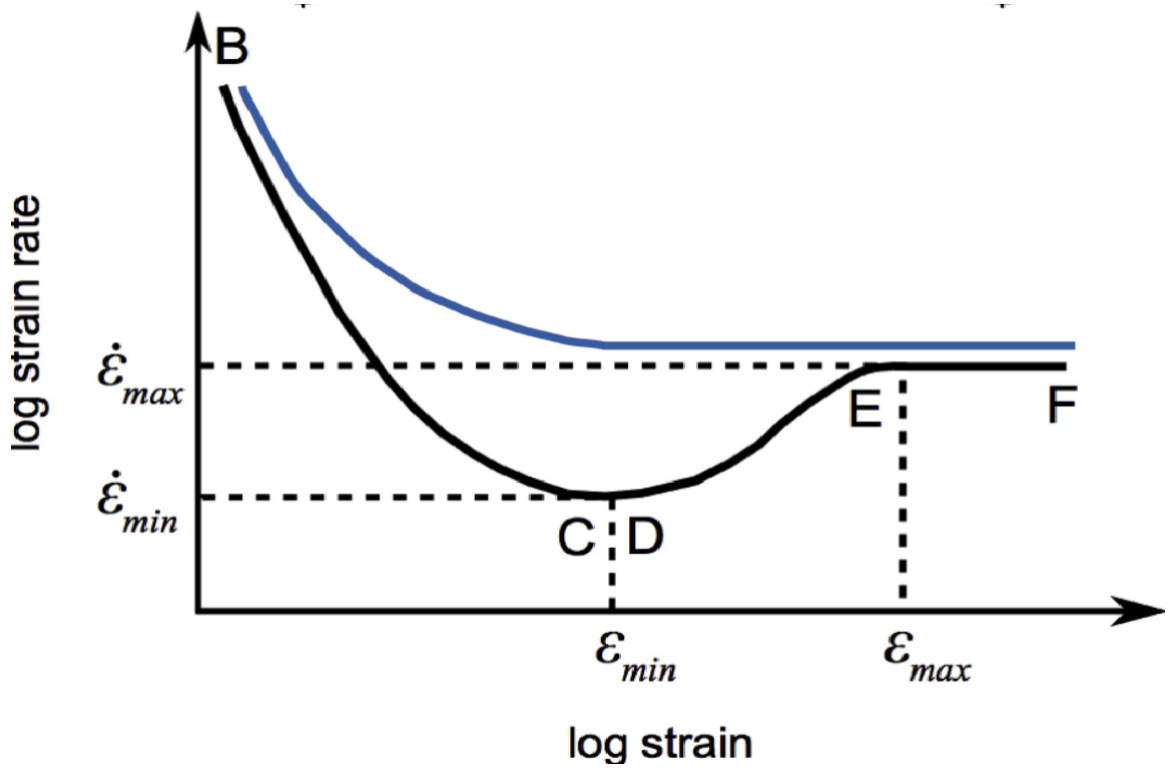

Figure 1.2: strain graph as adapted from (Faria et al., 2014b)illustrating the strain curve

the temperature of D_2O and H_20, we will be referring to Hexagonal Ice (1h) in the whole project whenever ice is mentioned.

Ice can be considered as a rock or as a mineral because of its crystalline nature. It exists on earth at a very high homologous temperature usually above 0.9 Which makes it behave in a way that is similar to the behaviour of rocks close to their melting point. When ice is subjected to stress, like most rocks, it displays a wide range of mechanical response depending on the magnitude of stress as well as strain rate and temperature and pressure applied (Wilson et al., 2014). Schematically, the typical history of stress in polycrystalline ice during sustained loading can be illustrated as in figure 1.2 which shows the graph of the log of strain rate over log of strain as adapted from (Faria et al., 2014b). He submitted that the time graph of deformation for ice is not a straight line graph as earlier submitted by other authors. At low stress level, when the elastic limit is not exceeded, ice shows an instantaneous elastic response and is a creeping ductile material. The behaviour depends on the rate of deformation and deformation history. But at high stress and strain rates, ice is extremely brittle which may fail by brittle fracture as a result of the formation, propagation and nucleation of cracks(Schulson & Duval, 2009)

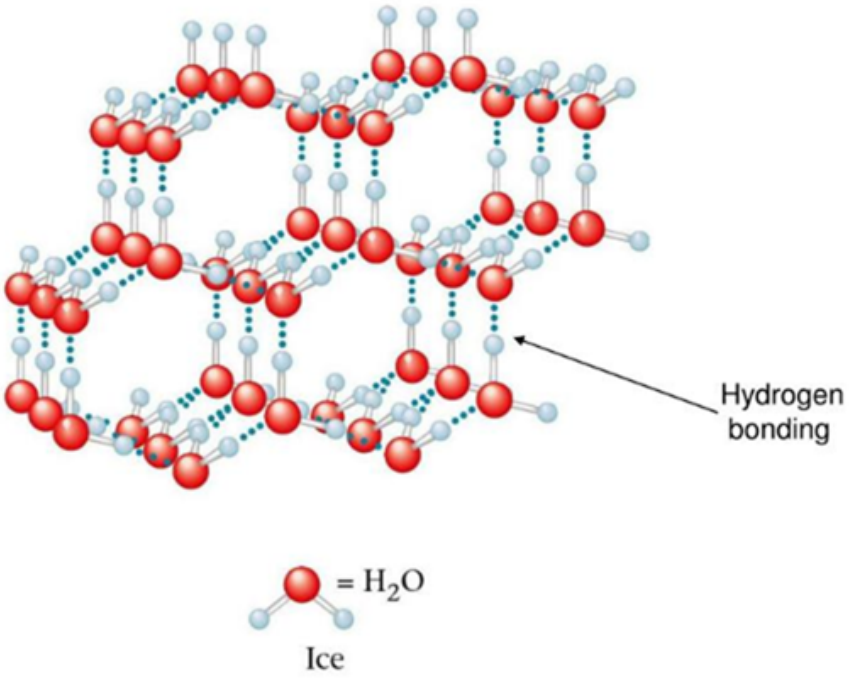

Figure 1.3: Hexagonal structure of crystalline ice with oxygen atom bonded together by hydrogen bond (Pauling, 1935)

1.2.1 Microstructure

The basic mechanical properties of ice is essentially determined by the microstructure and behaviour of individual crystals and the orientation relative to one another in a polycrystalline aggregate (Petrenko & Whitworth, 1999; Staroszczyk et al., 2019). The ice crystal has hexagonal symmetry and belongs to the group of same hexagonal crystal family of minerals which include Cadmium, Magnesium, Titanium and Zinc. Crystalline ice is described above is formed from cooling of liquid water molecules(in this case D_2O) to temperature below 0^0C so that it possesses a repeating tetrahedron coordination of oxygen atoms. Where the oxygen atoms are situated at each of the vertices of the hexagonal rings and the edges of the rings are formed by hydrogen bonds.

Figure 1.3 Illustrate the hexagonal structure of the ice crystal with oxygen atom bonded together by hydrogen bond (Pauling, 1935). For a typical ice crystal, Planes parallel to the crystal hexagonal bases are called basal planes, the lateral sides of the crystals are called the prismatic planes and the direction perpendicular to the basal plane is refereed as the optic axis or the c-axis. The orientation in space of the c-axis is very important as it defines the various properties of the ice. A closer insight into the microstruture of ice crystal reveals that the hexagonal rings are not perfectly planar . The six oxygen atoms are arranged in two parallel planes so that three oxygen atoms are in each of the planes with alternating atoms in the upper and lower planes

(Staroszczyk et al., 2019). The Distance between any of pair of such planes in which oxygen atoms forming a hexagonal ring is equal to 0.0923nm, which is much less than the distance separating the adjacent distance of 0.276nm separating adjacent pairs of planes (Staroszczyk et al., 2019). When viewed along c-axis direction, the consecutive parallel planes in the oxygen atoms are arranged in an alternating pattern so that they are mirror image of each other. Ice crystals are usually of extreme purity, irrespective of the composition of water from which they are formed since only few chemical substances are able to fit into the ice crystal lattice (Staroszczyk et al., 2019). The grains are of random shape and are approximately of similar sizes and may consist of up to several crystallites. Grains in turn form larger structures called polycrystals which in general contain many grains varying in shape, size and orientation. When the orientation of individual crystal c-axes in a polycrystalline aggregate are distributed at random,then the polycrystal can be considered macroscopically isotropic otherwise it displays some form of macroscopic anisotropy. As individual ice grains in a polycrystal are stressed due to applied loading, they deform themselves and interact with each other in a way that depends considerably on how the crystal basal planes are oriented to the stress field and on the anisotropy of the crystal. The crystal c-axes in turn gradually rotate in response to the stress configuration giving rise to the evolution of preferred orientation of c-axis or fabric. This also leads to formation of melt in the grain boundary in response to the stress field

In the first instance, once a sample is stressed , the grains deform in a purely elastic and reversible way similar to a metal within its elastic limit. This is done by lengthening or shortening of atomic bonds, this can be referred as bulk instantaneous elastic strain(Faria et al., 2014b; Staroszczyk et al., 2019). On the same hand, as a result of shear stress generated between grains through the sliding taking place on the grain boundary. This sliding is accommodated by elastic deformation of the grain with no permanent deformation inside the grain. In other words, the crystal stores energy during deformation and this energy can be recovered if the applied compressive stress is relaxed. Dislocation glide, is another form of deformation that happens on a grain. These deformation takes place in characteristics discrete bands parallel to the crystal basal plans. This irreversible creep deformation is enhanced by the presence of point defects in the crystal lattice.

1.2.2 Grain boundary

Grains can be defined as regions of uninterrupted crystalline lattice which is separated from other regions by a grain boundary. Though such regions are not perfect, there could be localized distortion of lattices caused by defects and this dislocation can arrange themselves into a stable structure called subgrain boundaries (Faria et al., 2014b).

These grain boundaries are regions of defect and are know to contain water in glaciers especialy at three grain boundary. Nye, 1989 experimental research suggested that polycrystalline ice in equilibruim at melting point has water at liquid phase situated at three grain junction.

1.3 Network Analysis

INTRODUCTION TO PORE NETWORK ANALYSIS

The importance of fluid flow in a geo-dynamic settings cannot be overemphasised because of its essence in the storage of radioactive waste management which is one of the most presssing need for the world (Xiong et al., 2016). Fluid flow is important in characterization of resevoir properties in the petroleum industry and tracking environmental waste for hydrologist. Understanding of fluid flow helps in the successful tracking of hyrdothermal fluid because successful development of hydrothermal ore systems requires an appropriate geodynamic settings to generate metal fertile fluid reservoirs, it also requires also the generation of permeable fluid pathways to drain the fluid from potentially large volume fluid reservoirs. These pathways are a result of destruction and creation of pores and microcracks as the rock undergoes deformation (Cox et al., 2005). Several investigation has been conducted on pore scale level to characterize the size and shape of the pores (Schmitt et al., 2016) and comparing the shapes of the pores to artificial artifacts. The mass transfer through porous media depend on the structure and nature of the pore geometry and the (Schmitt et al., 2016; Wiedenmann et al., 2013) Knowledge of the pore morphology, flow law are essential to help model the appropriate system in play in each geo-dynamic settings. This has led to extensive studies on pore scale properties of materials in order to understand how Darcy's law controls transport through porous media.

There has been different approaches to pore scale modelling ranging from Lattice-Boltzmann(LB) models, smoothed particle models,direct numerical simulation model, percolation model, pore network model to imaging technique model. With the advances in material imaging especially in X-ray Computed Tomography(XCT), Neutron Tomography (NT) together with increase in computational power and increased interest in observing macroscopic behavior of materials on pore scale, has made researchers to resort to 3D imaging and Network Modelling. Pore network models has been an effective tool used to investigate and predict macroscopic properties from fundamental pore-scale behaviour of processes and phenomena based on geometric volume averaging. It is a mechanistic model that utilizes an idealization of the complex pore space geometry of the porous media. This is usually done by representing the pore space by

pore elements having simple geometric shapes such as spheres, cylinders for the pore body and pore throat. (Al-Raoush & Willson, 2005; Celia et al., 1995).

There have been two main approaches for estimation of pore network parameters: the forward and backward methods. The forward methods are based on the microscopic 2-D or 3-D imaging followed by morphological analysis and image processing in order to extract the network properties. The backward methods observe the macroscopic characteristics of porous media which is then used to calculate the pore network. The most critical part in constructing a pore network is defining its structure which includes determination of pore body size and distribution, pore body locations, pore throat size distribution, connectivity and the spatial correlation between pore bodies (Al-Raoush & Willson, 2005; Rabbani et al., 2017; Thompson, 1997). With the above understanding it is feasible to predict the porosity, permeability and drainage characteristics of a body of study. Pore bodies are usually represented by spheres whose size and distribution is representative of pore bodies found in the medium of interest, while the pore throat is represented by cylinders with an analogous size distribution that is characteristic of the narrow openings that connect the pore bodies. (Jivkov et al., 2013; Sheppard et al., 2006). The connection between two pore bodies is the fundamental parameter in network modelling as it helps to estimate various other parameter like the permeability and drainage characteristics and hydraulic conductance(Rabbani et al., 2017).

1.3.1 Pore throat/Coordination Number

Shah et al., 2016 defined Pore network coordination number as number of pore throat which are connected to a pore. Spatial correlation is the network structure of the sample defined by pore body correlation, Body-throat size correlation and the average pore body radius to the average pore-throat radius in the system. Coordination number is also the number of pore throat connecting to each pore body while the pore throat is the local constriction connecting two pores.

1.3.2 Pores

Pores in ice are volumetric defect which is formed as a result of rejection of oxygen and nitrogen from the lattice of water during solidification (Schulson & Duval, 2009). It contains only air when it is made from fresh water and brine with other impurities when it is made from salt water. Pores can be connected like in the case of firn or isolated as in ice. In the study of Pore morphology, Pores is said to be open when the pores are connected to the surface of the sample or core or closed when it is otherwise. Pores are usually represented by elements having simple geometeric shapes such as spheres in 2D and ellipsoid in 3D this is to enhance the modelling of a proper pore

geometry. Using GeoDict predicts the pore size of a pore space by fixing a sphere into the pore space to obtain the best fit. A voxel is part of a pore with a diameter equal or larger than D, if it is included in the sphere of diameter D, which is completely included in the pore space. The superposition of all spheres with diameter D that can be included in the pore space is equal to the pore volume of all pores of diameter D or larger

Permeability

It has bee argued for that melting happens at the boundary of the solid or at defect in the solid (Lliboutry, 1971; Sawyer, 2001), the temperature at which melting occurs usually depend on certain factors like stress, interfacial free energy, salt content of the liquid phase and the nature of the defect (Lliboutry, 1971), but in this experiment, the temperature is already predetermined, so the interest will be on the distribution of the melt in the whole sample. We know that heat is generated during deformation and the geothermal temperature at the base of the ice (Lliboutry, 1971) and the melt are found in the gain boundary (Nye, 1989; Sawyer, 2001) and this this thin film of fluid migrating through the base of the glacier.

1.3.3 Pore morphology

The dependence of pore morphology on ice temperature has proved to be a significant challenge to the study of the microstructural evolution of ice pores. More studies are needed to improve our understanding of the structure of pores of ice especially in three dimensional. We will like to begin the discussion on pore morphology by defining some aspects of it

1.3.4 Methods to obtain Pore-Network Structure from Three-Dimensional Images

Non- destructive direct imaging approaches are attractive because they provide a detailed and non destructive image of the pore space geometry. An important aspect of the process is that the connectivity and spatial variation in pore structure geometry are retained. Maximum Ball(MB) method and Watershed Method are two methods for pore network extraction from 3- dimensional images. The maximum ball algorithm calculates the dimensionless capillary pressures and can identify pore location within the pore network (Baychev et al., 2019; Dong & Blunt, 2009). The Maximum ball method also uses the Watershed method in identifying the pore throat. The watershed

Algorithm (WA) follows the basin principle where a drop of water falling on a topographic relief flows towards the nearest minimum which lies at the end of the steepest descent. (Sheppard et al., 2005)used the methods to analyse X-ray tomography images of rocks after Thompson et. al,., developed the method. The watershed method is divided into 3 major stages. The primary stage is the preparation of the 3D image for segmentation which involves euclidean transform and noise filtering. The second stage is to apply block distance transform to the pore spaces of the rocks followed by median filtering to avoid detection of prolate shapes (Baychev et al., 2019; Sheppard et al., 2006). The final stage is to gather information representing the extracted network. (Baychev et al., 2019)

2 Materials and Method

The following sections describes the samples and the methods used for the analysis. A brief introduction of the sample materials and processes is made for better understanding of the analysis.

2.1 Material Description

The Tomography images were acquired from cylindrical shaped core samples. Eight different sets of samples were analyzed but 3 sets of sample were selected and analyzed in order to be able to compare the microstructure of the sample before and after deformation. The cylindrical samples of D_2O ice were imaged using residual stress diffractometer Kowari at OPAL research reactor Bragg Institue ANSTO, Australia. The details of the analysis has already been reported previously in (Wilson et al., 2019; Wilson et al., 2020). The materials were made following the procedure for making standard Laboratory ice and the description of each of the samples is made in the sections below

Table 2.1: Boundary conditions and parameters for analysis

Sample Name	DH06	DH29	DH35
Strain Rate	$2.5x10^{-}6$	$2.5x10^{-}6$	$2.5x10^{-}6$
Temperature (^0C)	-7	-7	-7
Time(mins)	1460	1340	1325

2.1.1 Sample DH06

DH06 is made of a mixture of Liquid D_2O ice and 10% H_2O ice that was compacted before undergoing deformation. The undeformed has a voxel volume of 1600X1600X1701 with a voxel size of 20.4um. The voxel size of the deformed sample is 1600x1690x1551 with a voxel size of 20.4um.

2.1.2 Sample DH29

Like DH06,DH29 is consist of 90% D_2Oice and 10% H_2O ice.This sample is made of compacted bubble free ice matrix. Air bubbles were mechanically expelled by stirring

the mixture continuously and removing excess water by lightly compressing the mixture. DH29 has a voxel volume of 1500x1550x1851 and a voxel size of 20.36um while the deformed sample has a voxel volume of 1807x1700x1601 with the same voxel size

2.1.3 Sample LDH35

Sample LDH35 is composed of a mixture of D_2O and D_2O as the previous samples but with a thin lamina of fragmented Calcite mineral which was sandwiched in between the sample. Though because of similarity between the refractive index of D2O and calcite, it became difficult to distinguish the calcite component from the sample during segmentation.

2.2 Image Analysis

The application of Neutron Tomography Imaging to characterize geomaterial is based on grayscale values. The samples contains volume of empty space called void space while other composites are made of different materials with unique density represented by different gray scale value.

Image processing is a vital step after acquiring 3Dimages of samples. It forms the backbone of digital rock physics and helps to accurately predict properties of a complicated rock sample.

2.2.1 Image Segementation

Segmentation is the partitioning of a greyscale image into disjoint regions that are homogeneous based on their intensity values (Al-Raoush & Willson, 2005; Sheppard et al., 2006) Image segementation was done on the data in order to obtain a morphological representation of the different media system and to quantify the pore scale parameters such as porosity, different phases and pore network structure.

All samples were pre-segmented. At the same time, the pre-segmentation parameters were chosen so that the samples show as few artifacts as possible and do not lose any important information. The samples were all masked and cut using the Avizo 3D analysis software and filtered using the GeoDict software in the “Non-Local Means Filter” tool. The ”Non-Local-Means” filter is a powerful filter for reducing noise, for smoothing 3D images and for improving the display of edges.

Avizo is a commercial, high-performance 3D analysis and visualization software and was developed by Thermo Fisher Scientific. The software is used for interactive visualization, modeling, analysis and calculation of image data in an intuitive workflow.

The program is a versatile tool for understanding scientific and industrial data sets. Avizo 2019 Were used to process the scan series.

GeoDict, the "virtual material laboratory", is an innovative material simulator that provides a selection of algorithms to analyze virtual porous media. This modular software toolbox offers a complete solution for multi-scale 3D image processing, modeling and visualization. The computer-aided simulations enable a better understanding of the geometric and physical properties and can supplement or even replace laboratory measurements. GeoDict 2019 Was used to process the scan series.

The "grayscale thresholding" image segmentation of the scan series was carried out using the "Threshold" tool in the "Image Segmentation" module in Avizo. The pore space and the individual phases were selected manually using global segmentation in the multiple threshold. The associated threshold values of the phase boundaries for each sample and the individual phases are listed in the appendix.)

The watershed transform image segmentation was performed on the sample to partition the sample into different phases.The sample was partitioned into six different phases based on their intensity. Calcite, D2O,H2O all appeared as a distinct phase while HDO appeared as three different phases based on its own binary intensity.

2.2.2 Pore Size Distribution

The Pore Size Distribution (PSD) was obtained by the segementation of reconstructed 3Dimage into pores and grains. The GeoDict uses the Maximum ball method algorithm to determine the size of a pore and its geometry. With a voxel size of 20.4um, the pore radius was determined by fitting spheres into the pore space. And a Point belongs to a pore of radius R, if it is inside any sphere of radius r, which can be fitted into the pore space. The graph of the pores size distribution is presented in figure...

The pores are classified by their diameter into bins that have the bin size entered in the box. All bins are of equal size and each contains pores with diameter in the range $[(i-1)xBinsize]$ and $[ixBinsize]$ and i being the bin number which is 2.03644um in this case. Different samples where analyzed, Table 3.1 shows the different samples and parameters for the analysis.

The Granulometry calculates the isolated pores inside the structure with no connectivity or accessibility that can be identified and measured. The pores were then classified by their diameters into bins according to the bin size entered in the box. The bin size were chosen to reflect the distribution of the pores and the grains. All bins are of equal size and each contained pores with a diameter in the range comprised in the bin range.

2.2.3 Identify Pores

Identify Pores was done in the following steps.segments the pores from the solid or other matrix in the following stages; first was to Initialize the sample by loading the presegmented image, then segmenting the Pore-Fragment and reconnecting any section that was over segmented. Second step was to set the Domain-boundary options and pore shape Analysis.

The Initialization Parameter segments the pores using the watershed algorithm but because the sample had alread been segmented, this was overcomed by loading pre-segmented data.

The Pore-Fragment Reconnection functions to reconnect over segmented pores from the watershed algorithm. With Pore-Fragment Reconnection, oversegmented pores are merged depending on the size of the shared interface and the merging of the connected pores which can be controlled using the values of interface threshold though the choice of the interface threshold is adapted to the expected pore shape of the structure.

Domain-Boundary options defines the boundary of the pores touching the domain boundary after the segmentation and pore fragment reconnection have been done. This helps to improve the results.

Pore-Shape Analysis is done by fitting ellipsoids into the identified pores . this is done after the pore has been identified , reconnected and domain boundary established.

3 RESULTS

3.1 Qualitative Description

The analysis was performed with 90% D_2O and 10% H_2O ice for sample DH06 and DH29 and with 10% fragmented calcite for the LDH 35 sample. Together with the compressive deformation, the temperature of the samples was increased from -7^0C to 2^0C. The partial melting causes the H2O to go into a liquid form making it easy to flow and to react readily with D_2O ice. This also causes more mixing as more of the hydrogen ion from H_2O mixes with the Deuterium ion to form a new mineral HDO.

The initial stage of the melting begins at triple grain junction and edges where the grains are in contact with each other. With increase in stress the melt increases and form isolated pockets of fluid developing a reactive front line as illustrated in figure 3.1. When the degree of compaction increases, leading to decrease in solid volume fraction and increase in the melt pockets. Thus these melt pockets enlarges and gets connected to the neighbouring melt pocket to form interconnected melt network. Once such a network is established, the partial melt system is permeable; melt can then move out of the solid framework. Whether or not the melt move depend on the driving force to squeeze it out and the dilatant site for it to collect in. If the partially melted rock is subject to hydrostatic stresses, the melt fraction does not leave the solid matrix, but in the case of deviatoric stress, the melt will be pushed out of the solid matrix as it deforms.

To observe the movement of fluid in the samples, we segmented the samples into different components to enable us analyze each component of the sample before and after deformation. The segmentation processes yielded 6 different components of the sample and they include: Pores, D2O, Mix1, Mix2, Mix3 and H2O. Figure 1 illustrate the different components with their different colours to enable readers follow the discussion more properly. In the figures that follows, pores will be illustrated with red colour, D_2O with Dark gray, Mix1 with green, Mix2 with blue, Mix3 with Purple while H_2O is illustrated with yellow. It is worth noting that Mix1, Mix2, Mix3, are different grade of HDO which resulted from the introduction of D_2O liquid into H_2O ice crystals during the formation of the samples. The intensity of hydrogen ion and deuterium ion increases on either side. For this analysis, the deformed sample was used to characterize the pores and Microstructure in order to obtain deformation structure. The image

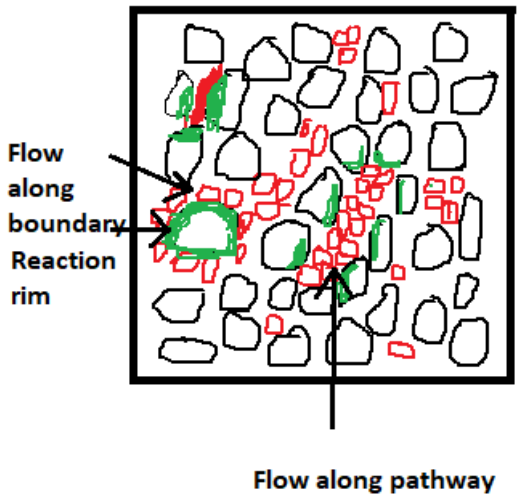

Figure 3.1: Sketch illustrating the flow of water through the grain boundary and connected pores

Figure 3.2: Chart illustrating the different colours for different components

resolution for the study is 20.4um which allows for the pores and other components to be visualized properly in the reconstructed images.

FIg 3.3 displays the reconstructed image of DH06 with a volume of 1600 X 1600 X 1701 a voxel resolution of 20.4um. In the analysis, the whole volume of the sample was used in other to understand the distribution of the different components before and after deformation. The deformed sample has a voxel volume of 1600 X 1690 X 1551

Sample DH29 has a reconstructed volume image of 1500 X 1550 X 1851 with same voxel size as DH06 while the deformed sample has image volume of 1807 X 1700 X 1601. Fig 3.4 is the 3D image rendering of sample with the different components illustrated in different colour as described in previous section.

Sample LDH35 is composed of a mixture of D_2O and H_2O as the previous samples but with a thin lamina of fragmented Calcite particles which was sandwiched in

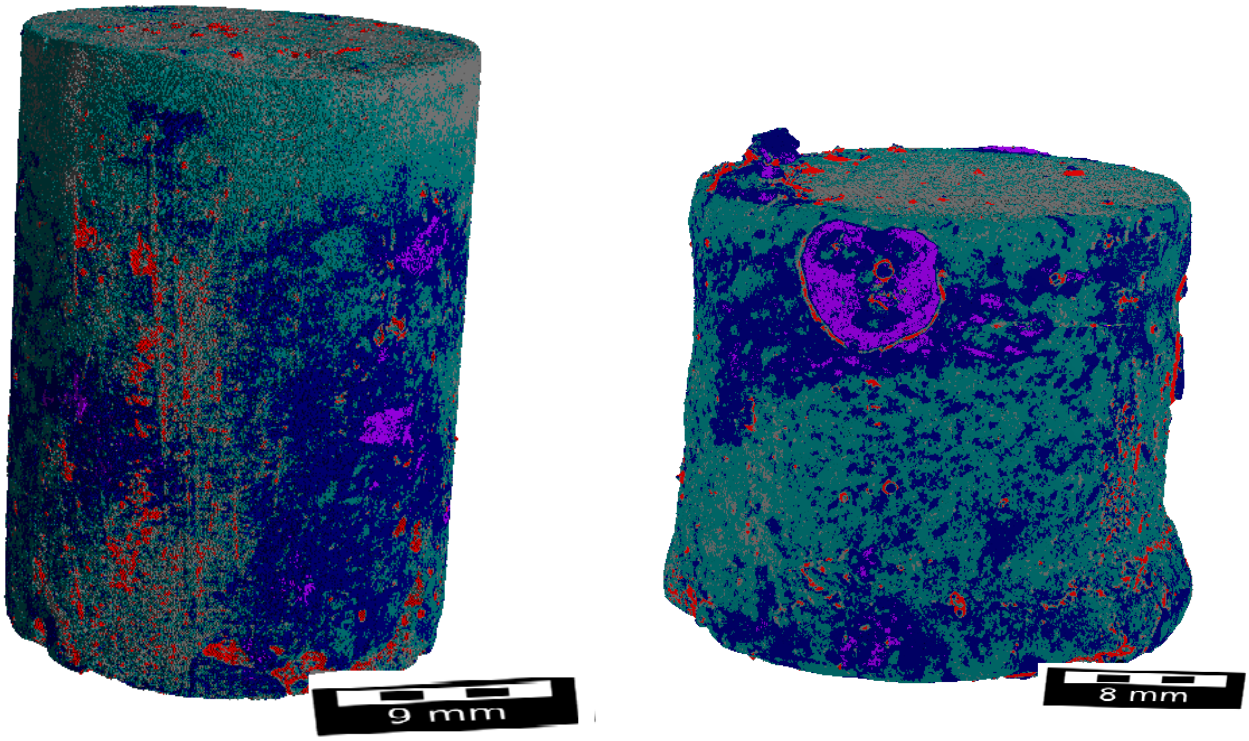

(a) (b)

Figure 3.3: 3D image rendering of sample 06 (a) before (b) after deformation

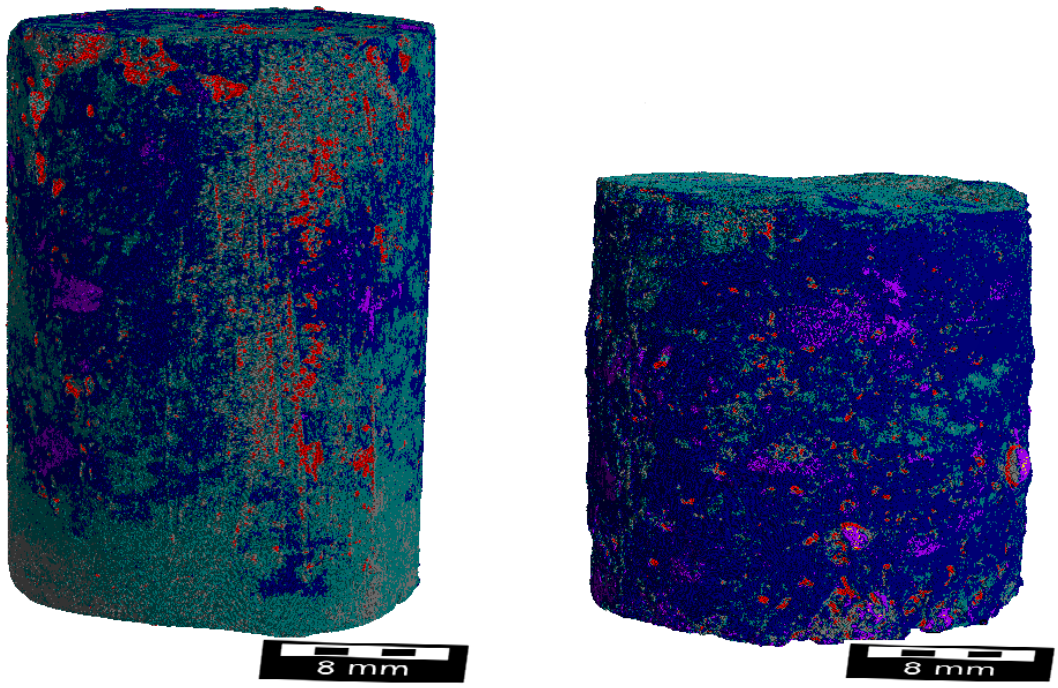

(a) (b)

Figure 3.4: (a) 3D image rendering of sample 29 (b) 3D image rendering of the deformed sample

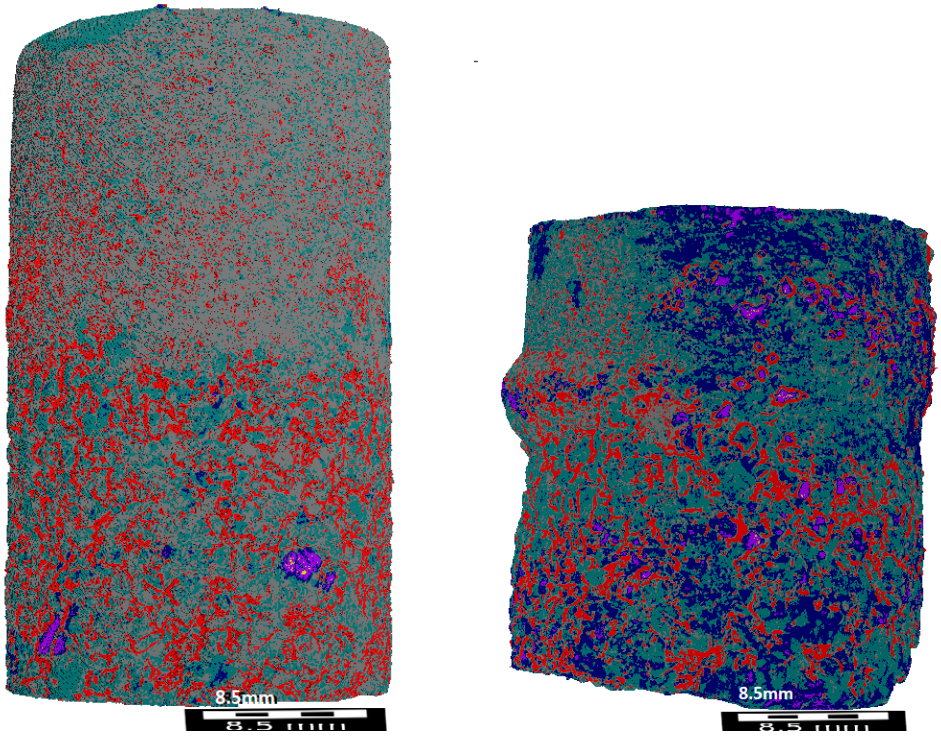

(a) (b)

Figure 3.5: (a) 3D image rendering of sample 35 (b) 3D image rendering of the deformed sample

between the sample. Though because of because Calcite has similar refractive index with D_2O, it was difficult to distinguish the calcite component from the sample during segmentation. The Sample has a total reconstructed image of 1650 X 1650 X 2327 with image resolution of 20.4um while the deformed sample has a voxel volume of 1600 x 1650 x 1751 The 3D image rendering of sample LDH35 and LDH35def is show in figure 3.5

3.1.1 Cross Sectional view of the samples

With the GeoDict cross sectional slides of the sample can be cut to have a good view of microstructural differences in the samples. This section illustrates the cross sectional view of the samples as the slide are cut in the same orientation and axis both for the undeformed and deformed sample.

The undeformed (Figure 3.6) sample have more dispersed pores especially at the upper part of the sample with little patches of the mixture (HDO). The deformed sample does not show much difference in structure except for the coalescing of the pores and more random distribution of the pores. The deformed sample showed less alteration by the deformation process.

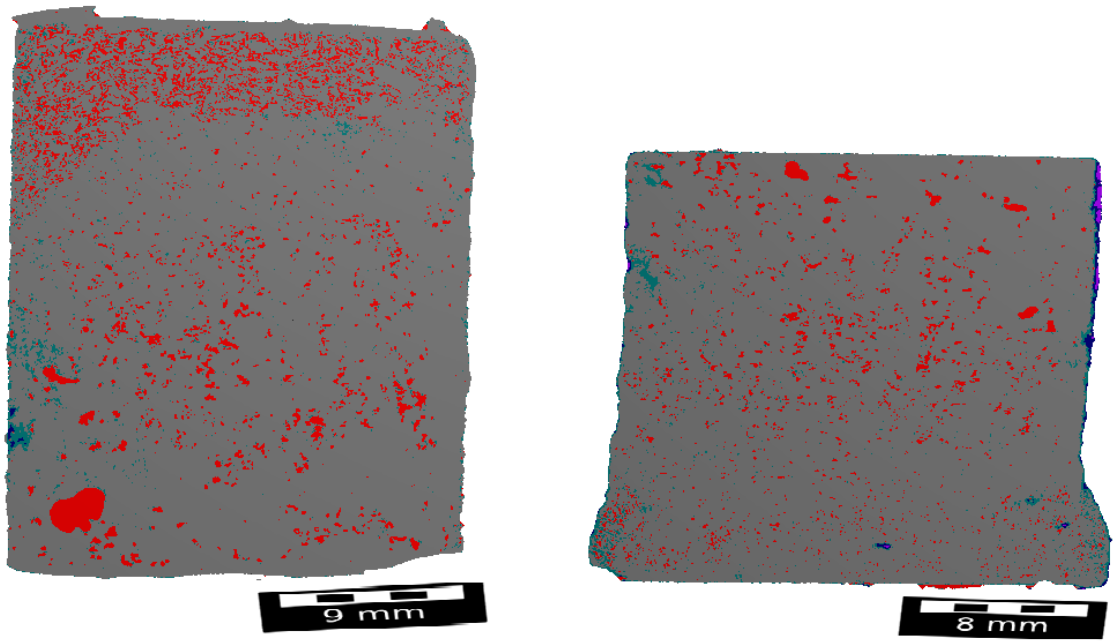

(a) **(b)**

Figure 3.6: Image rendering of sample DH06 (a) before (b)after deformation image

The undeformed sample figure 3.7 (a,c) showed the distribution of reactant fluid Without any flow while the deformed sample figure 3.7 (b,d) showed distribution of flow in the sample. The most pronounced of the flow structure being the flow along the fractures. Sample DH29 was highly compacted and bubble free sample which made reaction in the sample much more pronounced. During compaction, the different grains of the sample get strained at different rate due to the anisotropic nature of the ice crystals leading to the formation of dialation zone on the weaker zone. As the melt in the grain undergoes stress, they are forced to migrate to the dialation zone. The direction of flow is usually dependent on the resultant stress in this case the resultant stress resulted in the formation of a hybrid extensional fractures.

The undeformed sample (figure 3.8:a,c) has the pores and D2O matrix distributed in the upper part of the sample while the matrix of the melt are distributed on the lower part of the sample similar to distribution in the deformed sample. The lower part of the sample shows the distribution of the melt while the upper part has the distribution of the D2O matrix and the pores like in the undeformed sample. This is can be attributed to the effect of compaction having more effect at the base. The combined effect of the compressive pressure and lithologi pressure from the mixture and fragment of calcite. This resulted in the heterogenetic flow of the phases and formation of the phases along the hydraulic fractures. There are also evidence of flow in sample LDH35 (figure 3.8:a,b). Fibrous flow like sample 29 and more lateral flow

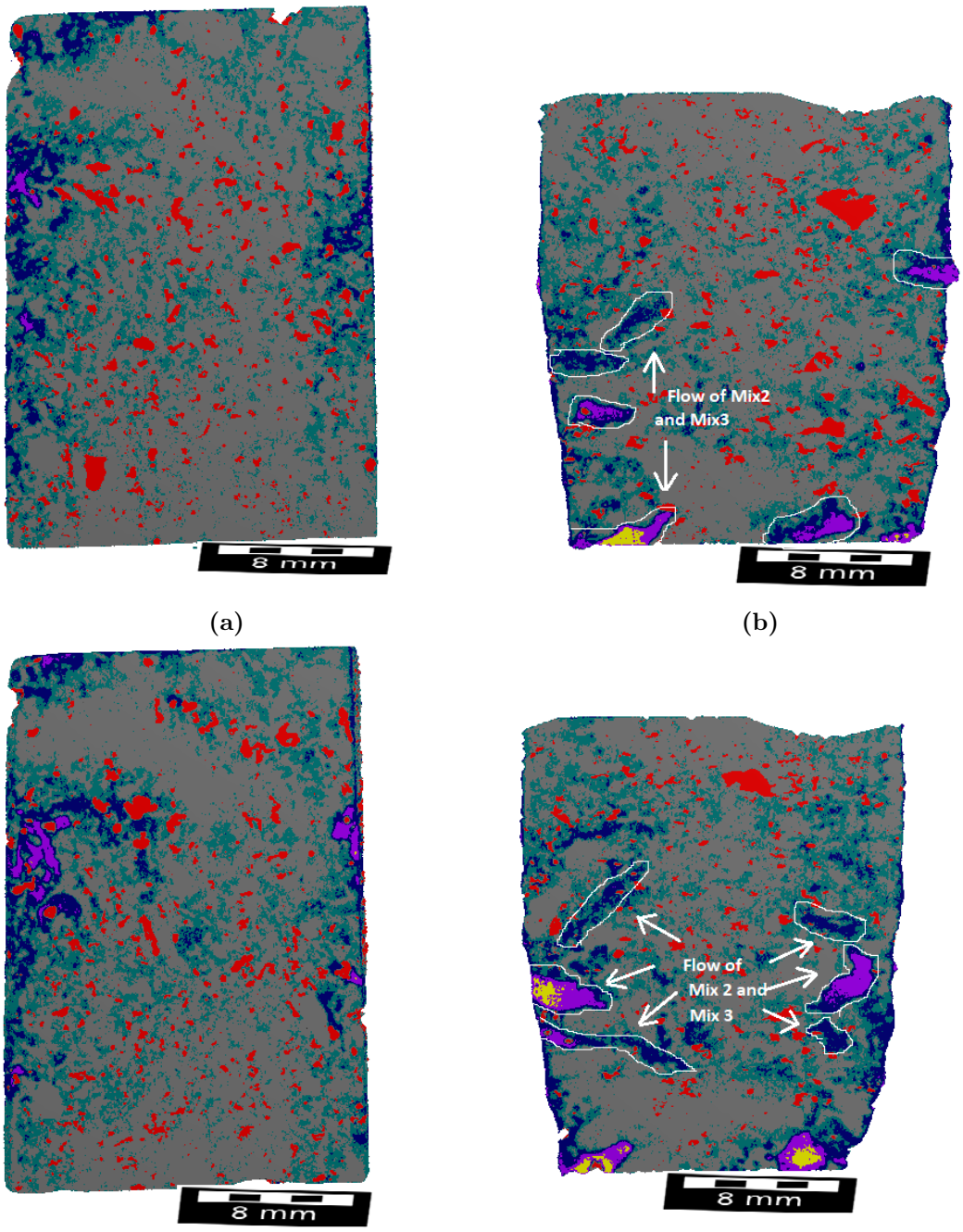

(a) **(b)**

(c) **(d)**

Figure 3.7: Image rendering of sample DH29 (a,c) before (b,d) after deformation. Observe that the phases were present in the undeformed sample but migrated during deformation and the structure was preserved once the sample was quenched by rapidly reducing the temperature to -7^0C

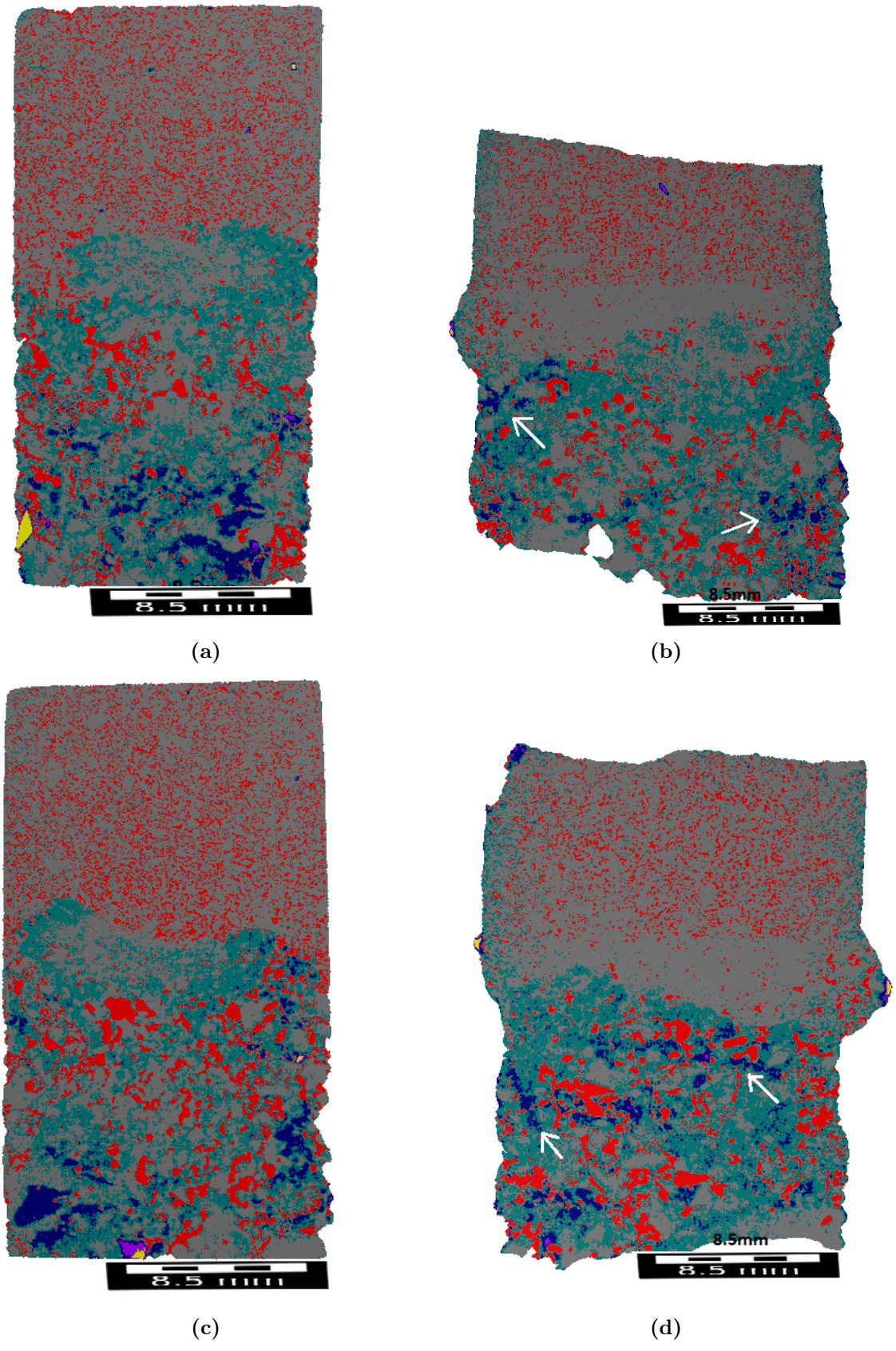

(a) **(b)**

(c) **(d)**

Figure 3.8: Image rendering of sample LDH35 (a,c) before (b,d) after deformation.

was identified in (figure 3.8:b) The lateral flow shows that the flow is within the First percolation Threshold (FPT)

3.1.2 Structure and preferred Orientation

This experiment gives a pronounced evidence of distribution of melt during deformation. The distribution can be described in grain scale. In The grain scale, Fluid in three grain junction usually develop a strong preferred orientation (Melt preferred orientation MPO) (Kohlstedt, 2002). This thin film of melt form along grain boundaries and the resultant minerals become rounded and appears as inclusion in the melt (Fig 3.7) forming a quadrangular shape with concave sides as illustrated in sample DH29 figure 3.7. This is usually because the Mix2 is still within the molten phase and has a higher temperature to migrate. The melt usually follows the path of the fracture created by the deformation process and or the site of dilation created by melt along the grain boundaries

As the compaction progress, the compaction pressure becomes greater than the intrinsic pressure in the sample, this is accompanied with dilation and fracturing affecting the rate of dilation which is dependant on the supply of the fluid. The combined effect of these processes propagate the porosity upward relative to the reaction front. As the rate of compaction increases especially at the base of sample, the porous zone increases in the vertical extent isolating the porous zone from the reaction front. Figure 3.7 This resulted in lateral displacement of the mixture phases upwards The fluid flow can be laminar as illustrated in figure 3.8(b) especially if the fracture is less than 250um(Walther & Orville, 1982) otherwise it flows the fracture zone and escapes at possible fissure. Among other things, the pressure gradient in excess of the hydrostatic pressure in the vertical direction is the main drive for the fluid in the vertical direction

Flow of fluid does not occur in all partially molten rocks. Sample DH06 shows little texture of deformation and flow. this could be attributed to the large and angular pores in the sample as illustrated by the mean coordination number

3.2 Topology and Pore Characteristics

In comparing the network topology of the deformed and undeformed samples, it will help to look at some characteristics of the pore network such as the pore size distribution, the network coordination number and the Sphericity histogram. The network coordination numbers show in a histogram the number and distribution of the pore throat while the the pore size distribution curve illustrates the distribution of the

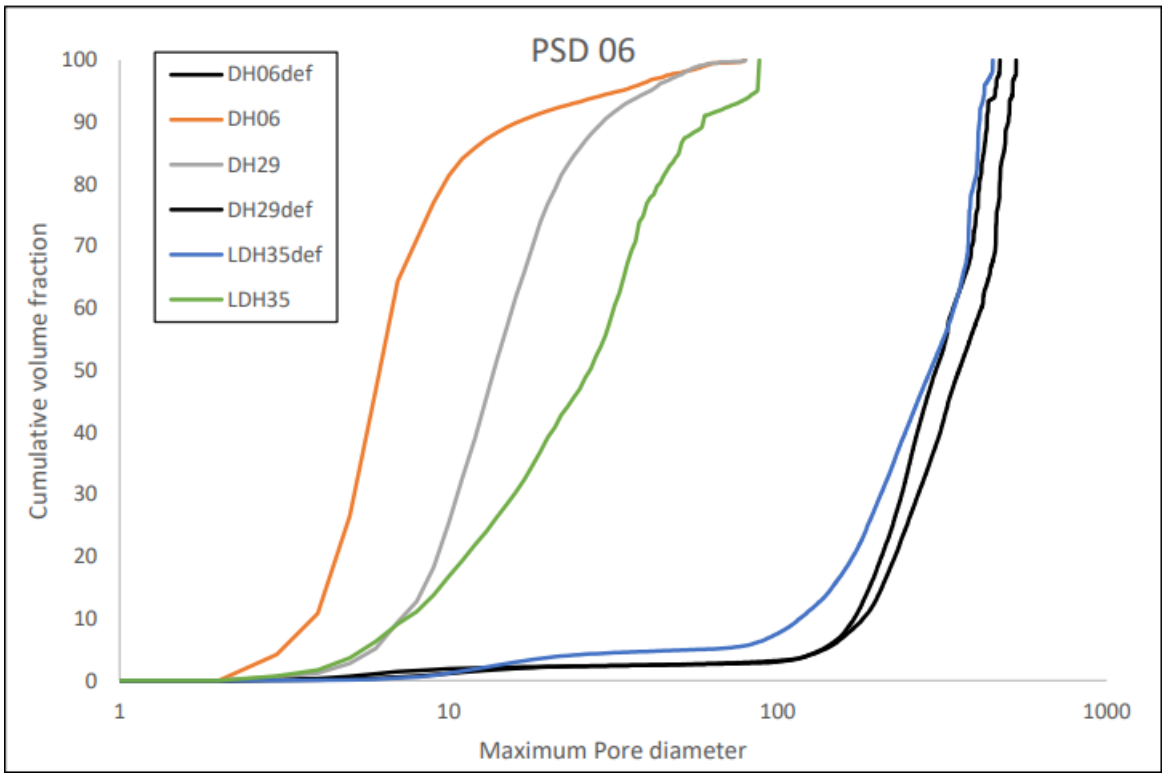

Figure 3.9: Cumulative plot of log of the maximum volume to the cumulative volume fraction

pores with their sizes and the sphericity illustrates in fraction how spherical the pores are within a ratio of 0 to 1.

3.2.1 Pore Size Distribution

The Pore Size Distribution (PSD) was obtained from the reconstructed 3D image of pores and grains. The cumulative volume fraction of the sample was plotted against the maximum diameter of the pores to show a representation of the pores. Porosimetry has the advantage of measuring isolated pores which mostly are not reachable from the exterior of the sample and therefore is necessary in computing essential parameters like porosity and pore connectivity. It provides graphical model displays both of the closed and open pores and provides an opportunity to observe the presence of closed pores in the sample (Figure 3.9). The resolution of the scanned image, is also a key factor of the direct imaging method used in this experiment. Since the the resolution of the image is 2.4um per pixel, it means that the minimum detectable pore is 20um.

In comparing the the curves, we observe that the detected pore diameters are within the same range though the distribution is different. This is because the method maps the internal topology of the porous medium by fitting in spheres into the pores. The resulting curves have a large number of points with each point representing pores of

different diameters. The curves also increases in the Y-axis as the volume of the pores increases while the shape of the curves changes with the nature of the pores. The deformed sample shows more larger pore sizes than the undeformed sample. Figure 3.9 shows the 3D volume rendering of the pores of the different samples. The curves shows a clear distinction between the pore distribution of the undeformed samples and the deformed samples as the deformed developed in size and volume. A weak relation is developed among the pores of the undeformed sample as they tend to have similar variation while the deformed sample tend to follow same direction.

3.2.2 Porosity

The segemented samples are divided into different components and voxels count for different samples are computed. Using the voxel count the macro-porosity was calculated by finding the ration of the pore component to the ratio of the total volume component of the whole sample. The macro porosity which is composed of both the closed and open pores was calculated by computing the ratio of the volume of the voxels of the pore to the total volume of the sample. Table 4.1 presents the list of the porosity as calculated using the voxel count. We compute the porosity of the three samples before they were deformed, and after they were deformed using the volume of the different components (D_2O,H_2O,MIX1,MIX2,MIX3).

Table 3.1: Table illustrating the different porosity in percentage

Sample	DH06	DH06def	DH29	DH29def	DH35	DH35def
Porosity	7.7	4.1	6.6	4.3	17	11

It is interesting to note the difference in porosity after deformation. The three samples analyzed and discussed in this report shows a considerable difference in porosity after deformation. DH06 has a porosity of 7.7and a porosity of 4.1 for the deformed sample which represents approximately 46 percent decrease after deformation. DH29 has a porosity of 6.6 percent before deformation and a porosity of 4.3 after deformation which represents about 35 percent decrease in porosity after deformation. It is worth noting that DH29 represent a compact sample with less bubble during production. DH35 not surprisingly has the highest porosity of 17 before deformation and 11 after deformation representing about 35 percent decrease in porosity.

3.2.3 Network Coordination Number

The Mean Network Coordination Number has significant influence on the overall characteristics of porous network. It shows how connected the pores are in a given sample.

Table 3.2: Table for the Mean Coordination number

Sample	DH06	DH06def	DH29	DH29def	DH35def
Mean Coordination number	2.4	0.9	0.7	0.6	2,0
Maximum coordination number	23	15	17	14	34

h!

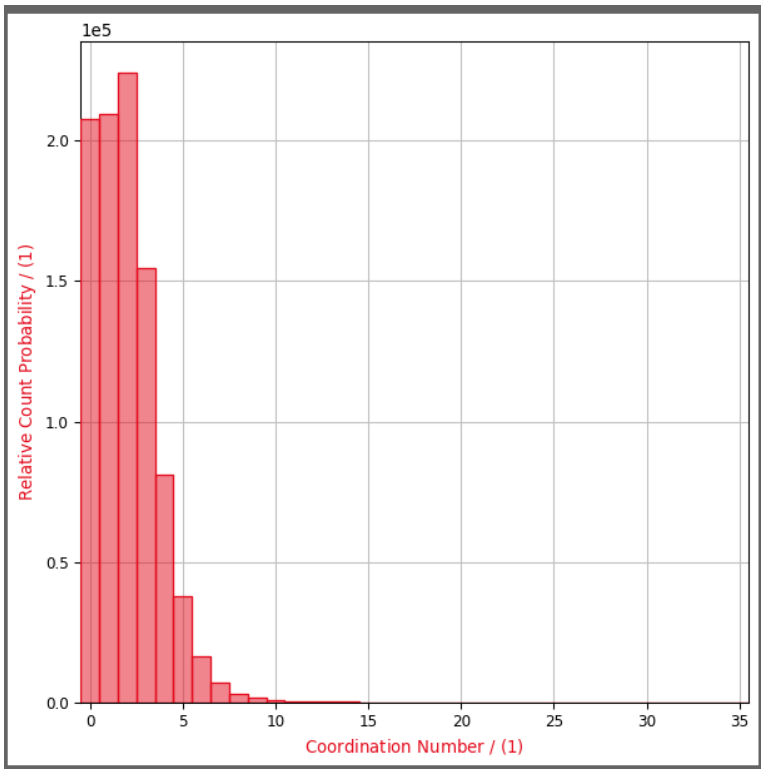

Figure 3.10: The graph of the coordination number of LDH35def. The high mean coordination number being a result of the intergranular calcite sandwiched within the sample

The distribution of coordination number for 3 set of samples are shown in Table 2. from the distribution the mean coordination number for sample DH06 undeformed is 2.4 and a maximum distribution of 23.The high coordination number could be attributed to irregularity of the of the pores as illustrated from the graph of the sphericity. This can be compared with the reduced coordination number of the deformed sample 0.9 and a maximum distribution of 15. Fig 11 (a,b) is a graph of the coordination number of both the undeformed and deformed samples of sample DH06 Sample DH29 has a similar number of both coordination number and maximum distribution of the sample DH06 figure 11(c,D) while the undeformed sample has a value 0.7 and a maximum distribution of 14 and the deformed sample has a coordination number of 0.6 and maximum distribution of 17 for the coordination number. The deformed sample of LDH35 has a value of 1.9 for the mean coordination number and a value of 34 for maximum distribution. The coordination number can be compared to ellipsoid having strong friction (Manning, 2018) but well graded and more irregular particle packing

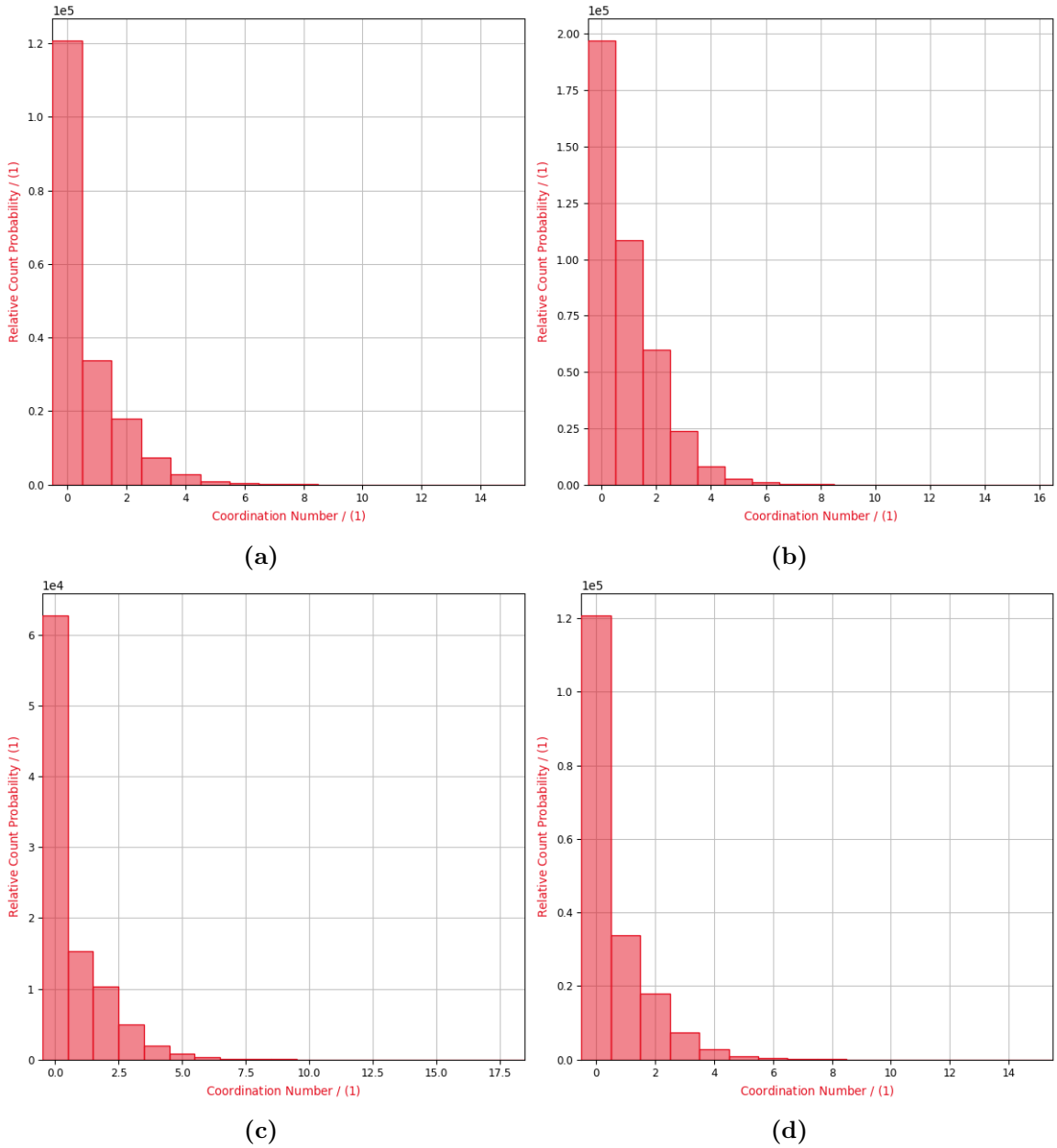

Figure 3.11: The Graph of the distribution of the coordination number for the sets of samples (a) coordination number for DH06 (b) coordination number for DH06def (c) coordination number for DH29 while (d) is the coordination number for DH29def.

have lower coordination value.

3.2.4 Sphericity

The sphericity is a 3D quantity is defined as the ratio of the surface of a sphere to the particle surface area obtained. The sheppard shericity was calculated by computing the ratio of the radius of the inscribed sphere to the raduis of volume of equivalent sphere. While Krumbein sphericity was calculated with the following formular $krumbeinsphericity = (bc/a2)1/3$ where a,b,c refers to the longest , medium and shortest diameter of the ellipsoid that have been fitted to the identifed pore. The sphericity is evaluated on the '0' to '1' ratio where 1 indicates that the pore is a perfect sphere. Figure 3.12 (a,b) shows the relative count probability of the sphericities of the pores of DH06 and DH06def illustrating the peak 0.04 and the degree of spread from 0 to 1. Figure 3.12 (c,d) shows the sphericity of DH29 and DH29def with both having same degree of spread and peak. Figure 3.12 (e,f) shows the sphericity of DH35def. The probability count for sample LDH35 peaked at almost 0.04 while that of the deformed sample peaked at 0.04 In all cases, it shows the reliability of the method to measure and account for spherical pores. Figure 3.13 is the Krumbein sphericity for the samples.

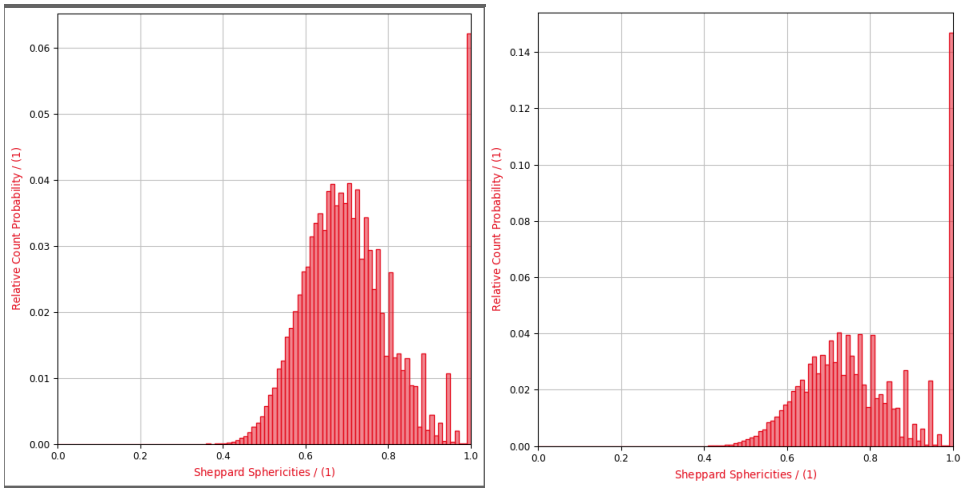

(a) DH06

(b) DH06def

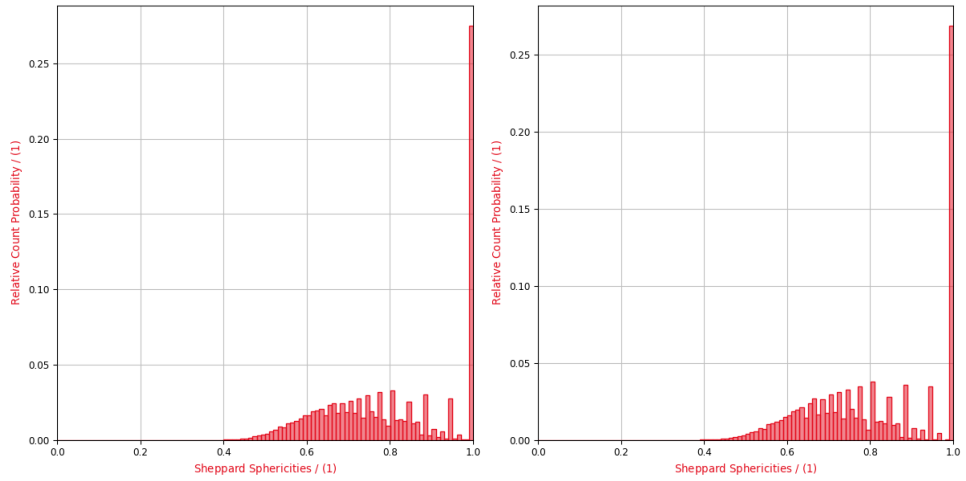

(c) DH29

(d) DH29def

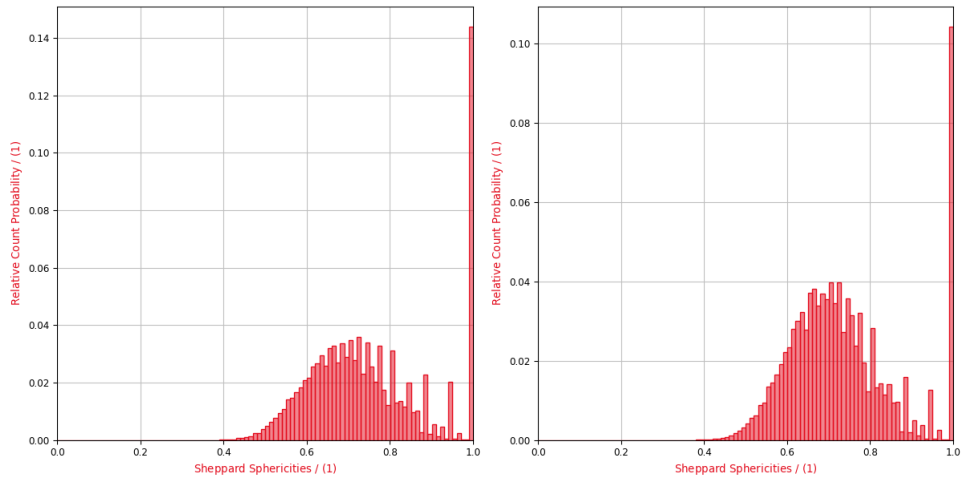

(e) LDH35

(f) LDH35def

Figure 3.12: Graph illustrating the sphericity of the set of sample (a) sphericity of DH06, (b) sphericity of DH06def, (c) sphericity of DH29, (d) shpericity of DH29def, (e) shericity of LDH35, (f) sphericity of LDH35def

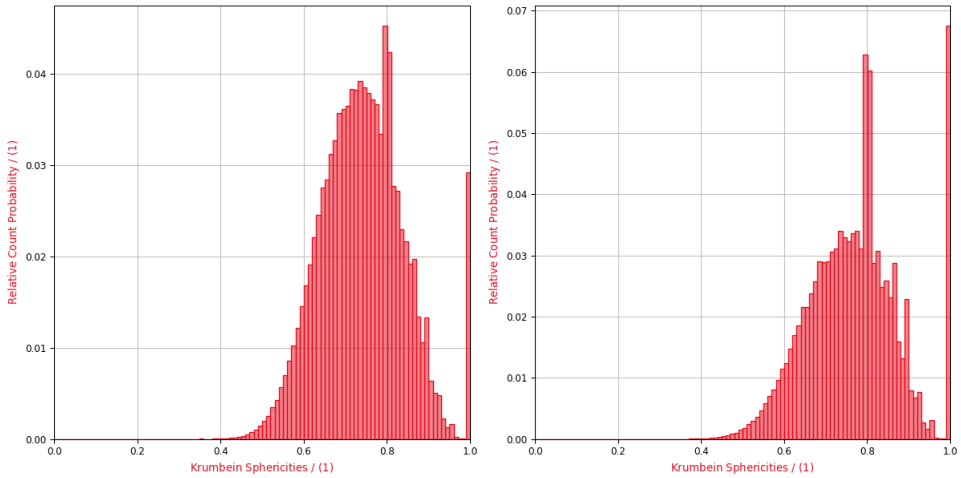

(a) DH06

(b) DH06def

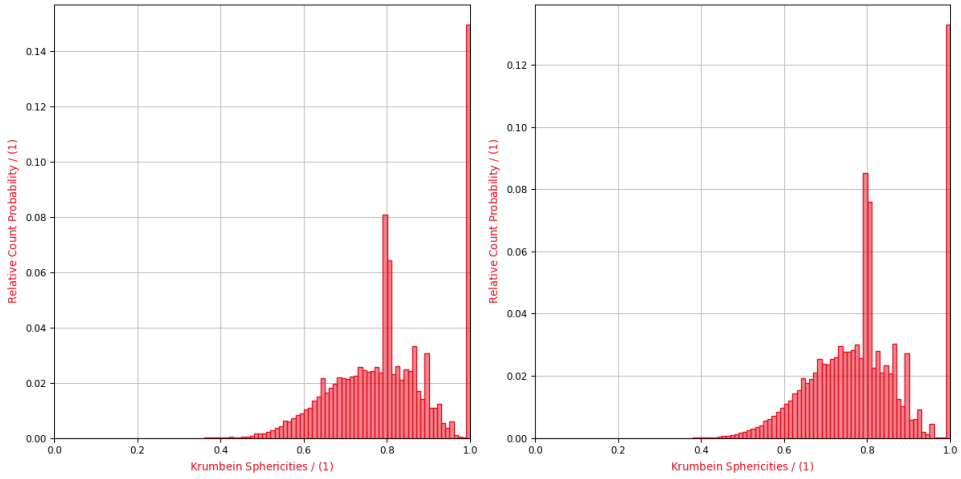

(c) DH29

(d) DH29def

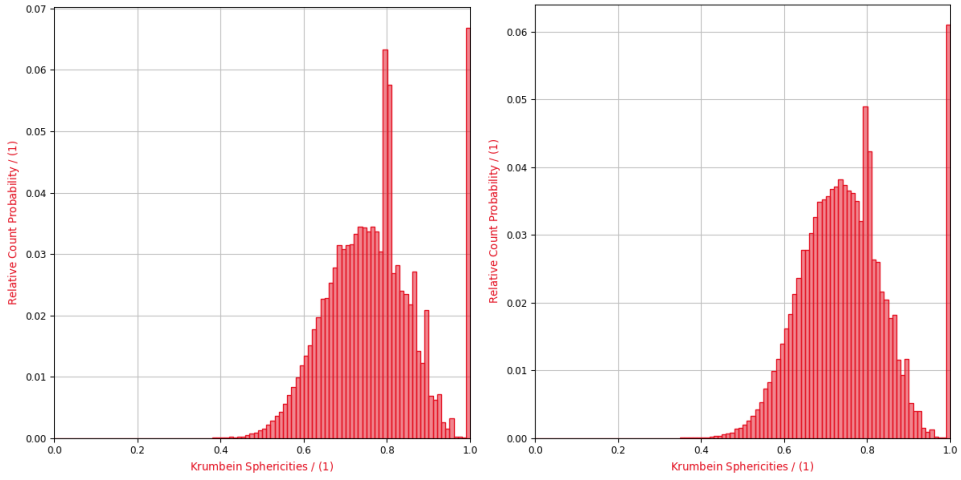

(e) LDH35

(f) LDH35def

Figure 3.13: Graph illustrating the Krumbein sphericity of the set of sample (a) sphericity of DH06, (b) sphericity of DH06def, (c) sphericity of DH29, (d) shpericity of DH29def,(e) shericity of LDH35, (f) shericity of LDH35def.

4 DISCUSSION

The study centered on observing the migration of fluid during deformation in an ice body by observing the movement of fluid in ice core sample. The samples were analyzed using Neutron Tomography Imagery and segmentation was done on the set of samples to identify different phases in the sample. The segmentation involved thresholding the gray images and distinguishing between pore space and the solid grains. Sheppard model was used in this analysis like in other analysis for porous rock (Baychev et al., 2019; Jivkov et al., 2013; Sheppard et al., 2005), The pore spaces are represented by spheres while the pore throat are represented pipes of circular cross section with corresponding hydraulic conductivity. The conductivity in this case is dependent on the viscosity of the fluid being transported and the morphology of the throat. The reconstructed image was used to monitor the different phases and to follow the structure of the deformed sample. It shows evidences for reactive fluid flow which is comparable to flow in metamorphic terranes. Fluid infiltration occurs during the ice sheet deformation which affect the ice body to depths even to the base of the ice (Lliboutry, 1968; Shreve, 1972). These fluid could be of varied sources which include meteoric fluids and fluids stored in the grain boundary which is at equilibrium temperature and pressure with the ice body.(Nye, 1989). The chemical and isotopic composition of this fluid are mostly defined by the salt content in the ice body and the flow through the large volume of the ice body. It is a major way through which the ice body is purified by eliminating the solutes stored at the grain boundary since the ice crystals is tiny to accommodate impurities, so most impurities are expelled to the grain boundary(Azuma et al., 2012).

4.0.1 Heat and mass transfer

The heat flow in this analysis led to increase in the reaction of the D_2O and H_2O mineral invariably leading to increase in production of the mixed phases. It also affects the driving force for the fluid and flow pattern by modifying permeability through recrystallization, porosity creation and formation of hydrofractures. The fluid flow then is an agent for mass and heat transfer during deformation because of the flux of the fluid within the ice structure. The significant heat transfer in most cases like in metamorphic terrane is by conduction whereas the mass transfer is by advection

(Bartels-Rausch et al., 2012; Bickle & McKenzie, 1987). The fluid flow transports heat by changing the thermal structure of the ice body thereby reducing the temperature as described by (Bell et al., 2014). The temperature gradient also has an effect on the flow by creating gradients in density and other properties of the fluid. This led to convection and buoyancy of less dense phases. The increase in the fluid pressure during the deformation processes are the major driving force for the fluid flow. The direction of flow can be heterogeneous in nature fig 3.6 so also the pattern and amount of fluid flow.

4.0.2 Structure and Geometry

The movement of the flow controls the resulting structures as can be observed from the reconstructed images. The movement of the fluid can be observed to not been focused into certain layers, this layers as the flow is still within the first pecolation threshold (FPT). Other structures that was observed in this analysis includes fractures and passive structures which were created by the fluid taking advantage of zones of high permeability or zones of enhanced reactions. The fluid orientation is usually along these direction. It becomes inclined if the fracture path is inclined.

4.0.3 Network Coordination Number

The result shows that the coordination number are different for each sample and they are consistent with coordination number by other authors(Baychev et al., 2019; Lindquist et al., 2000). However, they investigated the coordination number for a more porous meduim. The fluid migration in this analysis in enhanced mostly by the development of microcracks and fractures for the permeability of the fluid. The network coordination number in this analysis tends to decrease after deformation and for sample DH06 and DH29 peaked at zero suggesting network of isolated pores with coordination numbers of between 0.6 to 0.9. This is probably the rounding of the pores during deformation from the movement of the grains. The total porosity of the samples decreases after deformation. This is as a result of closing of some pores during the compaction process which is similar to findings of (Bernabe et al., 1982; Zhang et al., 1994).

5 SUMMARY

In order to study the movement of water through the microstructure of ice before and after deformation of the sample. Experiment was first conducted in Australia where the tomography was obtained. Segementation of the sample was conducted in Mainz Germany and the segmented section was analyzed using Geodict (the computer lab). Three distinct ice sample were systematically analyzed to characterize the pores based on segmented gray image from tomography analysis. The Pore size distribution of the undeformed sample was analzyed and compared with that of the deformed sample while the sphericity was used to analyze the type of pores obtained.

BIBLIOGRAPHY

Al-Raoush, R., & Willson, C. (2005). Extraction of physically realistic pore network properties from three-dimensional synchrotron x-ray microtomography images of unconsolidated porous media systems. *Journal of hydrology*, *300*(1-4), 44–64.

Azuma, N., Miyakoshi, T., Yokoyama, S., & Takata, M. (2012). Impeding effect of air bubbles on normal grain growth of ice. *Journal of Structural Geology*, *42*, 184–193.

Bartels-Rausch, T., Bergeron, V., Cartwright, J. H., Escribano, R., Finney, J. L., Grothe, H., Gutiérrez, P. J., Haapala, J., Kuhs, W. F., Pettersson, J. B., et al. (2012). Ice structures, patterns, and processes: A view across the icefields. *Reviews of Modern Physics*, *84*(2), 885.

Baychev, T. G., Jivkov, A. P., Rabbani, A., Raeini, A. Q., Xiong, Q., Lowe, T., & Withers, P. J. (2019). Reliability of algorithms interpreting topological and geometric properties of porous media for pore network modelling. *Transport in Porous Media*, *128*(1), 271–301.

Bell, R. E., Tinto, K., Das, I., Wolovick, M., Chu, W., Creyts, T. T., Frearson, N., Abdi, A., & Paden, J. D. (2014). Deformation, warming and softening of greenland's ice by refreezing meltwater. *Nature Geoscience*, *7*(7), 497–502.

Bernabe, Y., Brace, W., & Evans, B. (1982). Permeability, porosity and pore geometry of hot-pressed calcite. *Mechanics of Materials*, *1*(3), 173–183.

Bickle, M., & McKenzie, D. (1987). The transport of heat and matter by fluids during metamorphism. *Contributions to Mineralogy and Petrology*, *95*(3), 384–392.

Celia, M. A., Reeves, P. C., & Ferrand, L. A. (1995). Recent advances in pore scale models for multiphase flow in porous media. *Reviews of Geophysics*, *33*(S2), 1049–1057.

Cox, S. F. et al. (2005). Coupling between deformation, fluid pressures, and fluid flow in ore-producing hydrothermal systems at depth in the crust. *Economic Geology*, *100*, 39–75.

Dong, H., & Blunt, M. J. (2009). Pore-network extraction from micro-computerized-tomography images. *Physical review E*, *80*(3), 036307.

Faria, S., Freitag, J., & Kipfstuhl, S. (2010). Polar ice structure and the integrity of ice-core paleoclimate records. *Quaternary Science Reviews*, *29*, 338–351. https://doi.org/10.1016/.2009.10.016

Faria, S. H., Weikusat, I., & Azuma, N. (2014a). The microstructure of polar ice. part i: Highlights from ice core research [Microdynamics of Ice]. *Journal of Structural Geology*, *61*, 2–20. https://doi.org/https://doi.org/10.1016/j.jsg.2013.09.010

Faria, S. H., Weikusat, I., & Azuma, N. (2014b). The microstructure of polar ice. part ii: State of the art. *Journal of Structural Geology*, *61*, 21–49.

Glen, J. W. (1955). The creep of polycrystalline ice. *Proceedings of the Royal Society of London. Series A. Mathematical and Physical Sciences*, *228*(1175), 519–538.

Henning, S., & Ulrich, J. (1997). Description of the migration of liquid inclusions in growing crystalline layers. *Chemical Engineering Research and Design*, *75*(2), 233–236.

Jivkov, A. P., Hollis, C., Etiese, F., McDonald, S. A., & Withers, P. J. (2013). A novel architecture for pore network modelling with applications to permeability of porous media. *Journal of Hydrology*, *486*, 246–258.

Kingery, W., & Goodnow, W. (1963). Brine migration in salt ice. *Ice and snow: Properties, processes and applications, edited by: Kingery, WD*, 237–247.

Kohlstedt, D. L. (2002). Partial melting and deformation. *Reviews in mineralogy and geochemistry*, *51*(1), 121–135.

Lindquist, W. B., Venkatarangan, A., Dunsmuir, J., & Wong, T.-f. (2000). Pore and throat size distributions measured from synchrotron x-ray tomographic images of fontainebleau sandstones. *Journal of Geophysical Research: Solid Earth*, *105*(B9), 21509–21527.

Lliboutry, L. (1971). Permeability, brine content and temperature of temperate ice. *Journal of Glaciology*, *10*(58), 15–29.

Lliboutry, L. (1968). General theory of subglacial cavitation and sliding of temperate glaciers. *Journal of Glaciology*, *7*(49), 21–58.

Manning, C. E. (2018). Fluids of the lower crust: Deep is different. *Annual Review of Earth and Planetary Sciences*, *46*, 67–97.

Mehnert, K. et al. (1973). Initial melting at grain boundaries of quartz and feldspar in gneisses and granulites.

Middleton, C. A., Grindrod, P. M., & Sammonds, P. R. (2017). The effect of rock particles and d¡sub¿2¡/sub¿o replacement on the flow behaviour of ice. *Philosophical Transactions of the Royal Society A: Mathematical, Physical and Engineering Sciences*, *375*(2086), 20150349. https://doi.org/10.1098/rsta.2015.0349

Nye, J. (1989). The geometry of water veins and nodes in polycrystalline ice. *Journal of Glaciology*, *35*(119), 17–22.

Pauling, L. (1935). The structure and entropy of ice and of other crystals with some randomness of atomic arrangement. *Journal of the American Chemical Society*, *57*(12), 2680–2684.

Petrenko, V. F., & Whitworth, R. W. (1999). *Physics of ice*. OUP Oxford.

Pfann, W. (1955). Temperature gradient zone melting. *Jom*, *7*(9), 961–964.

Piazolo, S., Wilson, C. J., Luzin, V., Brouzet, C., & Peternell, M. (2013). Dynamics of ice mass deformation: Linking processes to rheology, texture, and microstructure. *Geochemistry, Geophysics, Geosystems*, *14*(10), 4185–4194.

Rabbani, A., Baychev, T. G., Ayatollahi, S., & Jivkov, A. P. (2017). Evolution of pore-scale morphology of oil shale during pyrolysis: A quantitative analysis. *Transport in Porous Media*, *119*(1), 143–162.

Sawyer, E. (2001). Melt segregation in the continental crust: Distribution and movement of melt in anatectic rocks. *Journal of metamorphic Geology*, *19*(3), 291–309.

Schmitt, M., Halisch, M., Müller, C., & Fernandes, C. P. (2016). Classification and quantification of pore shapes in sandstone reservoir rocks with 3-d x-ray micro-computed tomography. *Solid Earth*, *7*(1), 285–300.

Schulson, E. M., & Duval, P. (2009). *Creep and fracture of ice*. Cambridge university press.

Shah, S., Gray, F., Crawshaw, J., & Boek, E. (2016). Micro-computed tomography pore-scale study of flow in porous media: Effect of voxel resolution. *Advances in Water Resources*, *95*, 276–287.

Sheppard, A., Sok, R., & Averdunk, H. (2005). Improved pore network extraction methods. *International Symposium of the Society of Core Analysts*, *2125*, 1–11.

Sheppard, A., Sok, R., Averdunk, H., Robins, V., & Ghous, A. (2006). Analysis of rock microstructure using high-resolution x-ray tomography. *Proceedings of the International Symposium of the Society of Core Analysts*, 1–12.

Shreve, R. (1972). Movement of water in glaciers. *Journal of Glaciology*, *11*(62), 205–214.

Staroszczyk, R., Staroszczyk, & Buettner. (2019). *Ice mechanics for geophysical and civil engineering applications*. Springer.

Thompson, A. B. (1997). Flow and focusing of metamorphic fluids. *Fluid flow and transport in rocks* (pp. 297–314). Springer.

Walther, J. V., & Orville, P. M. (1982). Volatile production and transport in regional metamorphism. *Contributions to Mineralogy and Petrology*, *79*(3), 252–257.

Weikusat, I., Kipfstuhl, S., Faria, S. H., Azuma, N., & Miyamoto, A. (2009). Subgrain boundaries and related microstructural features in edml (antarctica) deep ice core. *Journal of Glaciology*, *55*(191), 461–472.

Wiedenmann, D., Keller, L., Holzer, L., Stojadinović, J., Münch, B., Suarez, L., Fumey, B., Hagendorfer, H., Brönnimann, R., Modregger, P., et al. (2013). Three-dimensional pore structure and ion conductivity of porous ceramic diaphragms. *AIChE Journal*, *59*(5), 1446–1457.

Wilson, C. J., Hunter, N. J., Luzin, V., Peternell, M., & Piazolo, S. (2019). The influence of strain rate and presence of dispersed second phases on the deformation behaviour of polycrystalline d 2 o ice. *Journal of Glaciology*, *65*(249), 101–122.

Wilson, C. J., Luzin, V., Piazolo, S., Peternell, M., & Hammes, D. (2015). Experimental deformation of deuterated ice in 3d and 2d: Identification of grain-scale processes. *Proceedings of the Royal Society of Victoria*, *127*(1), 99–104.

Wilson, C. J., Peternell, M., Hunter, N. J., & Luzin, V. (2020). Deformation of polycrystalline d2o ice: Its sensitivity to temperature and strain-rate as an analogue for terrestrial ice. *Earth and Planetary Science Letters*, *532*, 115999.

Wilson, C. J., Peternell, M., Piazolo, S., & Luzin, V. (2014). Microstructure and fabric development in ice: Lessons learned from in situ experiments and implications for understanding rock evolution. *Journal of Structural Geology*, *61*, 50–77.

Xiong, Q., Baychev, T. G., & Jivkov, A. P. (2016). Review of pore network modelling of porous media: Experimental characterisations, network constructions and applications to reactive transport. *Journal of contaminant hydrology*, *192*, 101–117.

Zhang, S., Cox, S. F., & Paterson, M. S. (1994). The influence of room temperature deformation on porosity and permeability in calcite aggregates. *Journal of Geophysical Research: Solid Earth*, *99*(B8), 15761–15775.